

Photonic Band Gap Effects in Two-dimensional Polycrystalline and Amorphous Structures

Jin-Kyu Yang¹, Carl Schreck², Heeso Noh¹, Seng-Fatt
Liew¹, Mikhael I. Guy³, Corey S. O'Hern^{4,2}, Hui Cao^{1,2}

¹ *Department of Applied Physics, Yale University, New Haven, CT 06520-8482*

² *Department of Physics, Yale University, New Haven, CT 06520-8482*

³ *Science & Research Software Core,*

Yale University, New Haven, CT 06520-8286 and

⁴ *Department of Mechanical Engineering and Materials Science,*

Yale University, New Haven, CT 06520-8286

(Dated: May 27, 2018)

Abstract

We study numerically the density of optical states (DOS) in two-dimensional photonic structures with short-range positional order, and observe a clear transition from polycrystalline to amorphous photonic systems. In polycrystals, photonic band gaps (PBGs) are formed within individual domains, which leads to a depletion of the DOS similar to that in periodic structures. In amorphous photonic media, the domain sizes are too small to form PBGs, thus the depletion of the DOS is weakened significantly. The critical domain size that separates the polycrystalline and amorphous regimes is determined by the attenuation length of Bragg scattering, which depends not only on the degree of positional order but also the refractive index contrast of the photonic material. Even with relatively low refractive index contrast, we find that modest short-range positional order in photonic structures enhances light confinement via collective scattering and interference.

I. INTRODUCTION

Over the past two decades photonic crystals (PhCs) have been studied intensely because of their ability to control light propagation and emission¹⁻³. A unique feature of PhCs is that they possess photonic band gaps (PBGs), within which optical modes are absent and light propagation is prohibited^{4,5}. A PBG is an optical analog of an electronic band gap in crystals. Typically, a PBG is formed via Bragg scattering of light by a periodic lattice. An alternative mechanism for PBG formation is evanescent coupling of Mie resonances of individual scatterers made of high-index materials, which can be explained using the tight-binding model frequently applied to electronic band gaps in semiconductors. Lattice periodicity or long-range order is not required, and thus many amorphous semiconductors display large electronic band gaps. PBGs also exist in amorphous photonic structures that consist of strong Mie scatterers such as dielectric rods or spheres⁶⁻¹⁰. These structures are termed photonic glasses¹¹, in analogy to glassy silica, which has an electronic band gap spanning the entire visible frequency range. Even without Mie resonance, Bragg scattering of propagating waves by local domains can produce PBGs in structures with only short-range positional order. For example, complete PBGs exist in photonic amorphous diamond structures—three-dimensional (3D) continuous random networks with diamond-like tetrahedral-bonding between particles¹². Recently hyper-uniform disordered materials with short-range geometric order and uniform local topology have been shown to possess large PBGs¹³. Unique optical features of amorphous media have also been investigated experimentally¹⁴. Despite these studies, little is known about the transition from PhCs to amorphous optical materials, *e.g.*, how does the density of optical states (DOS) evolve as the structural properties of the material change from ordered to amorphous? Is there a critical size of ordered domains in polycrystalline materials below which the system becomes optically amorphous? Answering the above questions will provide physical insight into PBG formation in structures lacking long-range order.

In fact, nature utilizes both crystalline and amorphous photonic structures for color generation¹⁵⁻¹⁷. Periodic structures are intrinsically anisotropic, thus the colors they produce are iridescent (*i.e.*, change with viewing angle). In photonic polycrystals, the cumulative effect of a large number of randomly orientated crystallites makes the color non-iridescent¹⁸. Photonic amorphous media can also produce vivid non-iridescent colors via short-range

structural order¹⁹. Although the refractive index contrast is usually too low to form PBGs in most biological systems, the interference of scattered light selects the color whose wavelength corresponds to the structural correlation length²⁰. Therefore, short-range positional order can significantly modify photonic properties^{21–23}, leading to unique applications²⁴.

This paper presents numerical studies of the density of optical states (DOS) as a function of positional order in polycrystalline and amorphous photonic materials. To avoid Mie resonances, we consider two-dimensional (2D) arrays of air cylinders in dielectric media, where the PBGs are formed for transverse-electric (TE) polarized light via Bragg scattering. We monitor changes in the spectral region of reduced DOS as a function of the structural correlation length. The depth of the dip in the DOS remains nearly identical to that for periodic structures as long as the ordered domains are sufficiently large. Once the average domain size decreases below a critical value, the depth of the dip tends to zero quickly. In contrast, the spectral width of the dip first decreases as the ordered domains shrink, but then increases when the domain size falls below a threshold value. We find that the dependence of the depth and width of the reduced DOS region on domain size ξ agrees quantitatively for different refractive index contrasts n after normalizing ξ by the attenuation length of Bragg scattering in a periodic structure. This allows us to identify the polycrystalline and amorphous optical regimes from the ratio of the domain size to the Bragg length. For amorphous media with low refractive index contrast, there is little reduction in the DOS, yet scattering is enhanced by short-range order, which results in stronger confinement of light and higher-quality (Q) resonances.

The paper is organized as follows. Section II describes the methods used to generate two-dimensional polycrystalline and amorphous photonic structures, as well as a detailed characterization of the degree of spatial order. Calculation and analysis of the density of optical states in these structures are presented in Section III. Section IV demonstrates the enhanced scattering and mode confinement in systems with short-range order. Finally we conclude in Section V.

II. STRUCTURE GENERATION AND CHARACTERIZATION

We first describe the numerical simulation methods to generate N cylinders of circular shape in a square box with periodic boundaries. For the purpose of generating configurations

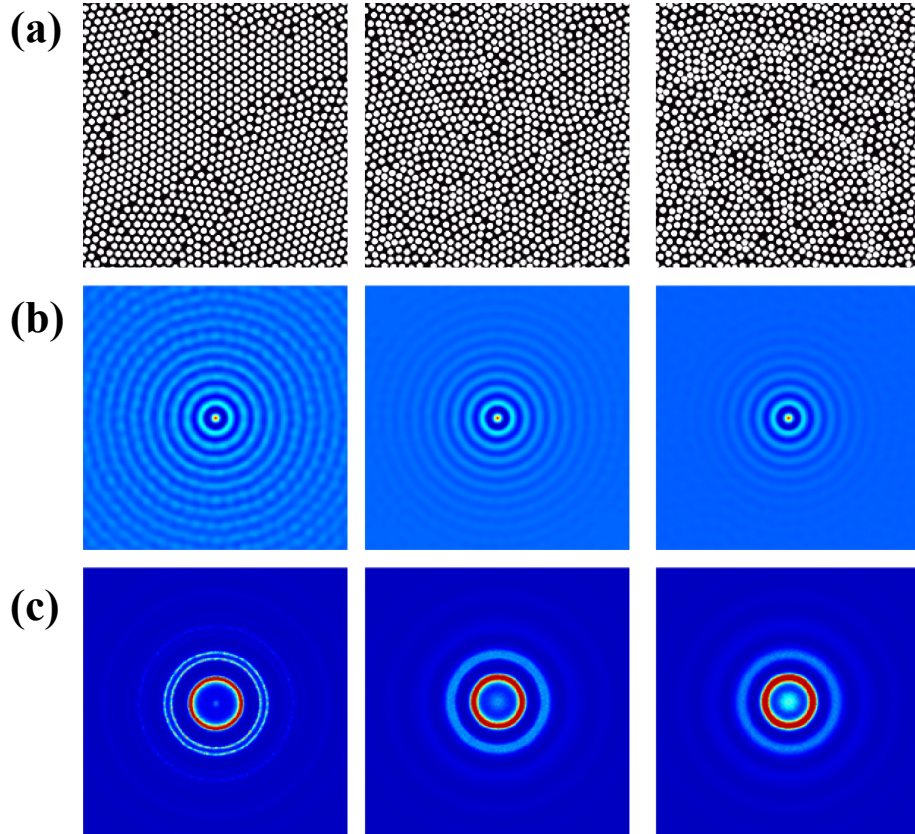


FIG. 1. (a) Typical configurations of two-dimensional arrays of air cylinders (white) in a dielectric host (black), generated using Protocol 1 described in Sec. II with polydispersity $p = 0.1$ (left), 0.3 (middle), and 0.5 (right). (b) Contour plot of the ensemble-averaged density spatial autocorrelation function $C(\Delta\vec{r})$ and (c) Power spectra $|f(\vec{q})|^2$ from Fourier transformed density for the same polydispersities in (a).

with varying positional order, we assume that the cylinders interact elastically via the purely repulsive short-range linear spring potential

$$V(r_{ij}) = \frac{b}{2} \left(1 - \frac{r_{ij}}{d_{ij}}\right)^2 \theta\left(1 - \frac{r_{ij}}{d_{ij}}\right), \quad (1)$$

where r_{ij} is the center-to-center distance between cylinders i and j , b is the characteristic energy scale of the interaction, $\theta(x)$ is the Heaviside function, and $d_{ij} = (d_i + d_j)/2$ is the average diameter of cylinders i and j . To vary the degree of positional order, the cylinders are polydisperse – with a uniform distribution of diameters between d_0 and $d_0(1 + p)$, where p is the polydispersity that ranges from 0 to 0.5. The average diameter $\langle d \rangle = d_0(1 + p/2)$.

Initially d_0 , or the packing fraction

$$\phi = \left(\frac{1}{L}\right)^2 \sum_{i=1}^N \pi \left(\frac{d_i}{2}\right)^2, \quad (2)$$

is set to a small value $\phi_0 = 0.2$, and we place N cylinders randomly within a square of side length L . We then gradually increase the diameters of all cylinders while maintaining the relative size distribution to create a jammed packing of cylinders²⁵. Each increment in diameter is followed by minimization of the total potential energy $V = \sum_{i>j} V(r_{ij})$ of the system. The energy minimization process is similar to moving each cylinder along the direction of the total force on it using overdamped dynamics. When V drops below a threshold value or the difference in energy between successive minimization steps is less than a small tolerance, the minimization process is terminated. If V is zero and gaps exist between cylinders, the system is unjammed, and it is compressed with a further increase of d_0 . If $V > 0$ after the energy minimization process, a large system-spanning number of cylinders are overlapped. To eliminate overlap, the system is decompressed, i.e., d_0 is uniformly decreased for all cylinders. The energy minimization process is repeated after the decompression step to find the local potential energy minimum. If $V = 0$, the system is compressed; if not, the system is decompressed again. The increment by which the packing fraction of the cylinders is changed at each compression or decompression step is gradually reduced to zero. Eventually when all of the cylinders are just touching and the net force on each cylinder is nearly zero, the system is considered “jammed”, and the process to increase the packing fraction is stopped.

For each polydispersity p , we generated at least 100 static, jammed packings of cylinders from random initial configurations. The values of ϕ are typically in the range between 0.82 and 0.85 with varying degrees of positional order. After generating jammed packings, we reduce the diameters of all cylinders to the same value (with $\phi = 0.5$) to eliminate the size polydispersity. Thus, in the final configurations, the structural disorder exists only in the positions of the cylinders with order decreasing monotonically with increasing p . Fig. 1 (a) shows the typical configurations of $N = 1024$ cylinders generated with $p = 0.1$ (left), 0.3 (middle), and 0.5 (right). For $p = 0.1$, the system contains several domains of cylinders with crystalline order, but each possesses a different orientation. With increasing p , the domains have reduced positional order and decrease in size.

To quantify the structural order, we calculate the ensemble-averaged spatial correlation

function of the density, the Fourier transform of the density, the radial distribution function $g(r)$, and the local and global bond orientational order parameters. The spatial autocorrelation function of density $\rho(\mathbf{r}) = L^{-2} \sum_{i=1}^N \theta(\mathbf{r} - \mathbf{r}_i)$ is given by

$$C(\Delta\mathbf{r}) = \frac{\langle \rho(\mathbf{r})\rho(\mathbf{r} + \Delta\mathbf{r}) \rangle - \langle \rho(\mathbf{r}) \rangle^2}{\langle \rho(\mathbf{r}) \rangle^2}. \quad (3)$$

$C(\Delta\mathbf{r})$ is averaged first over the spatial coordinates of the cylinders \mathbf{r} within one configuration, and then over at least 100 independent configurations. A contour plot of $C(\Delta\mathbf{r})$ is displayed in Fig. 1 (b) as a function of increasing p (from left to right) used to generate the configurations. For $p = 0.1$, $C(\Delta\mathbf{r})$ displays a large number of concentric rings and a modulation of the amplitude within a given ring, which indicates strong positional order. As p increases the system becomes more disordered and isotropic, since the number of visible concentric rings decreases and the amplitude within a given ring becomes more uniform. After integrating $C(\Delta\mathbf{r})$ over the polar angle, we plot in Fig. 2 (a) the peak amplitudes of the rings as a function of $\Delta r/a$, where $a = L/N^{1/2}$ is the average center-to-center distance between neighboring cylinders. The peak amplitudes decay more rapidly with Δr at larger p . The decay is approximately exponential, if we exclude the first peak near $\Delta r = a$. The faster decay from the first peak to the second arises from correlations induced by the just-touching jammed cylinders. The decay length ξ_r is extracted from the exponential fit $\exp[-\Delta r/\xi_r]$ of peak amplitudes after excluding the first peak. As shown in Fig. 2 (b), ξ_r is smaller for larger p , indicating the range of spatial order becomes shorter.

We also calculated the spatial Fourier transform of the structures, $f(\mathbf{q}) = \int d^2\mathbf{r} \exp[-i\mathbf{q} \cdot \mathbf{r}] \rho(\mathbf{r})$, where \mathbf{q} is the wavevector. Figure 1 (c) displays the ensemble-averaged power spectra $|f(\mathbf{q})|^2$ for $p = 0.1, 0.3$ and 0.5 , which consist of concentric rings. The radial width of the rings increases with p , as can be seen clearly for the first ring (with the smallest radius). The second and third rings are distinct for $p = 0.1$, which indicates the six-fold symmetry of the cylinders within each domain. For $p = 0.3$ and 0.5 , these rings become wider and merge together. We integrate $|f(\mathbf{q})|^2$ over all directions of \mathbf{q} to obtain the intensity as a function of the amplitude q . The inset of Fig. 2 (b) displays the intensity of the first ring versus q for $p = 0.1, 0.3$ and 0.5 . The center position of the peak q_0 gives the dominant spatial correlation length $s = 2\pi/q_0$. The peak becomes broader at larger p . The full width at half maximum (FWHM) of the peak Δq gives the average size of ordered domains $\xi_q = 2\pi/\Delta q$. As shown in Fig. 2 (b), ξ_q decreases with increasing p , similar to ξ_r .

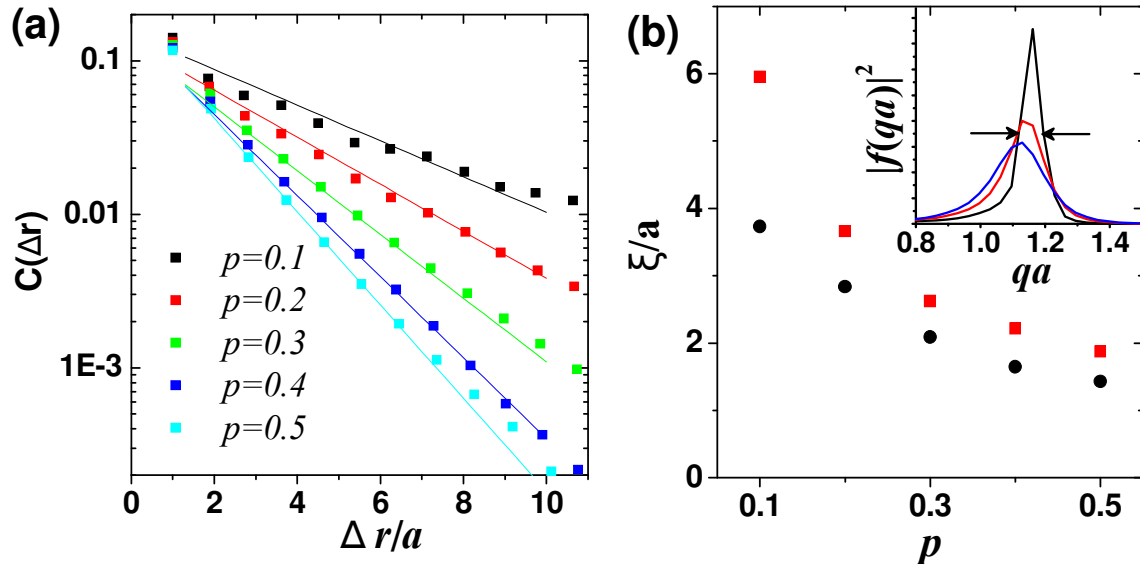


FIG. 2. (a) Logarithmic plot of the peak amplitudes for the ensemble- and angle-averaged density spatial autocorrelation function $C(\Delta r)$ for $p = 0.1, 0.2, 0.3, 0.4,$ and 0.5 . $a = L/N^{1/2}$ is the average distance between adjacent cylinders. The exponential fits of the data (solid lines) give the decay length ξ_r . (b) Inset: The first peaks of the angle- and ensemble-averaged Fourier transformed density $|f(qa)|^2$ for $p = 0.1$ (black), 0.2 (red), and 0.4 (blue), whose width gives the average domain size ξ_q . Main panel: ξ_r (circles) and ξ_q (squares) versus p .

The radial distribution function $g(r)$, plotted in Fig. 3 (a) for several values of p , gives the probability for a cylinder to be located a distance r from another cylinder at the origin relative to that for an ideal gas. The strong first peak, splitting of the second peak, and existence of peaks at large r for $p = 0.1$ indicate that the structure possesses crystalline order. With increasing p , the peaks are broadened, decay faster with r , and $g(r)$ resembles that for a dense liquid²⁹.

In addition to the translational order, we also characterized the orientational order of the configurations. The bond-orientational order parameter ψ_6 measures the hexagonal registry of nearest neighbors²⁶. ψ_6 can be calculated ‘locally’, which does not include phase information, or ‘globally’, which allows phase cancellations. Eqs. (4) and (5) provide expressions for the global and local bond-orientational order parameters in 2D structures.

$$\psi_6^g = \frac{1}{N} \left| \sum_{i=1}^N \frac{1}{m_i} \sum_{j=1}^{m_i} e^{6i\theta_{ij}} \right| \quad (4)$$

$$\psi_6^l = \frac{1}{N} \sum_{i=1}^N \frac{1}{m_i} \left| \sum_{j=1}^{m_i} e^{6i\theta_{ij}} \right|, \quad (5)$$

where θ_{ij} is the polar angle of the bond connecting the cylinder i to its neighbor j , and m_i denotes the number of nearest neighbors of i . Two cylinders are deemed nearest neighbors if their center-to-center distance $r_{ij} < r_{\min}$, where r_{\min} is the location of the minimum between the first two peaks in $g(r)$.

As shown in Fig. 3 (b), both ψ_6^l and ψ_6^g decrease as p increases. ψ_6^l is larger than ψ_6^g , because of the different orientations of the ordered domains. The error bars represent the standard deviations from 100 configurations. For $p = 0.1$, there is a significant fluctuation of ψ_6^g , because some configurations have only a few distinct domains while others contain many domains with different orientations. With increasing p , the number of domains N_d increases, thus the mean and standard deviation of ψ_6^g decrease. For $p = 0.5$, $\psi_6^g \approx 0$, the structures possess only local bond orientational order with $\psi_6^l \approx 0.55$ as found in dense liquids²⁶.

To check the sensitivity of the photonic properties on the protocol used for structure generation, we employed a second protocol that is very different from the first. Instead of constructing jammed packings at zero temperature, we generate equilibrated liquid configurations of cylinders at finite temperatures. ‘Liquids’ exist at finite temperature with nonzero root-mean-square velocities, thus the net force on each cylinder, arising from the repulsive interactions in Eq. 1, does not necessarily vanish. Employing molecular dynamics simulation methods, we simulated systems of cylinders at constant temperature over a range of packing fractions from $\phi_0 = 0.6$ to 0.8, which are lower than those obtained from the jamming protocol. The structures at higher ϕ_0 typically have more order, e.g., larger values of ψ_6^g . As in the first protocol, finally the diameters of all cylinders are reduced to a uniform value such that $\phi = 0.50$. Figure 4(a) shows two such configurations created using different initial packing fractions, $\phi_0 = 0.77$ (left) and 0.73 (right). The left (right) panel has $\psi_6^g = 0.80$ (0.27). Although the left structure possesses stronger global order, i.e. a higher value of ψ_6^g than most jammed structures generated with $p = 0.1$, its local order parameter ψ_6^l is smaller than most jammed structures at $p = 0.1$. This feature arises because in the liquid state nearest cylinders do not need to remain in contact as in jammed structures. In contrast to the first protocol, there are no well-defined domain boundaries in the structures generated by the second protocol as shown for the structure on the left in Fig. 1 (a).

Figure 4 (b) shows a plot of the average domain size ξ_q , extracted from the spatial Fourier

power spectra versus ψ_6^g for the structures generated by both protocols. The variation of ξ_q with ψ_6^g for both protocols agrees qualitatively.

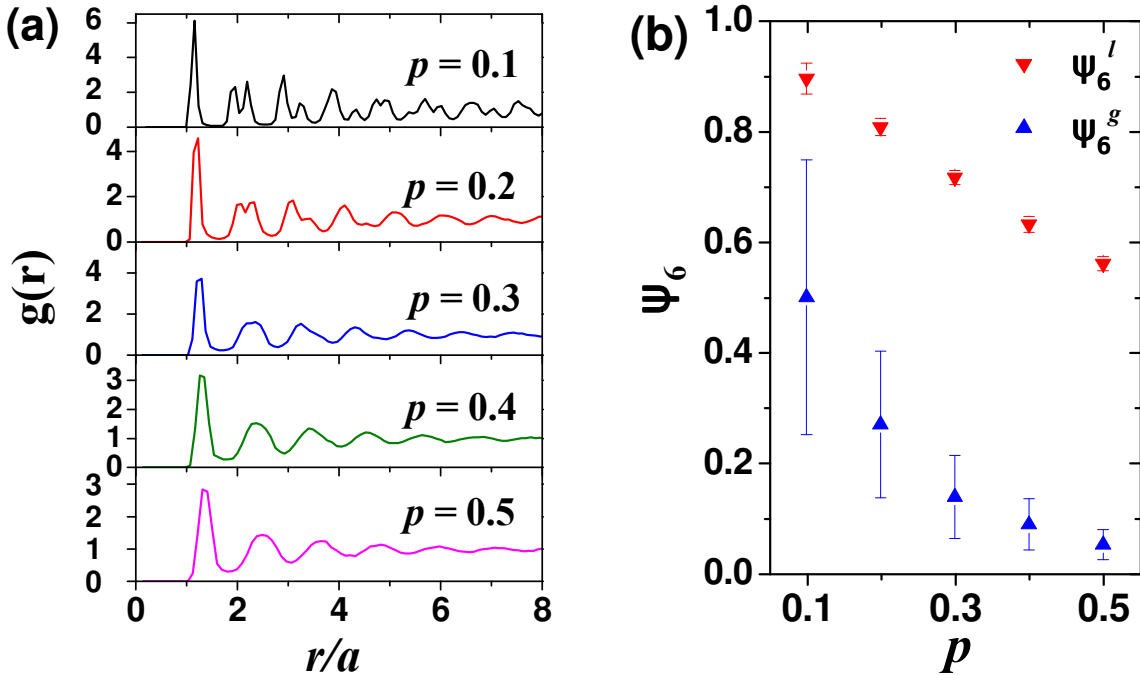


FIG. 3. (a) Radial distribution function $g(r)$ for $p = 0.1, 0.2, 0.3, 0.4,$ and 0.5 . (b) Local ψ_6^l (downward triangles) and global ψ_6^g (upward triangles) bond-orientational order parameters versus polydispersity p .

III. DENSITY OF OPTICAL STATES

We calculate the DOS with transverse electric (TE) polarization using the order- N method²⁷. The magnetic field is parallel to the axis of the air cylinders, and the electric field exists in the 2D plane. Since the cylinders are generated in a square with periodic boundary conditions, we can use it as a supercell for the DOS calculation. For the initial conditions, we choose a superposition of Bloch waves with random phases for the magnetic field and set the electric field to zero²⁸. The spectral intensities, averaged over many Bloch wave vectors and configurations, correspond to the DOS of the system under consideration. We tested our code by reproducing the DOS for two-dimensional photonic structures in the literature²⁸.

In Fig. 5, we plot the DOS as a function of the normalized frequency $\omega a/2\pi c = a/\lambda$ for

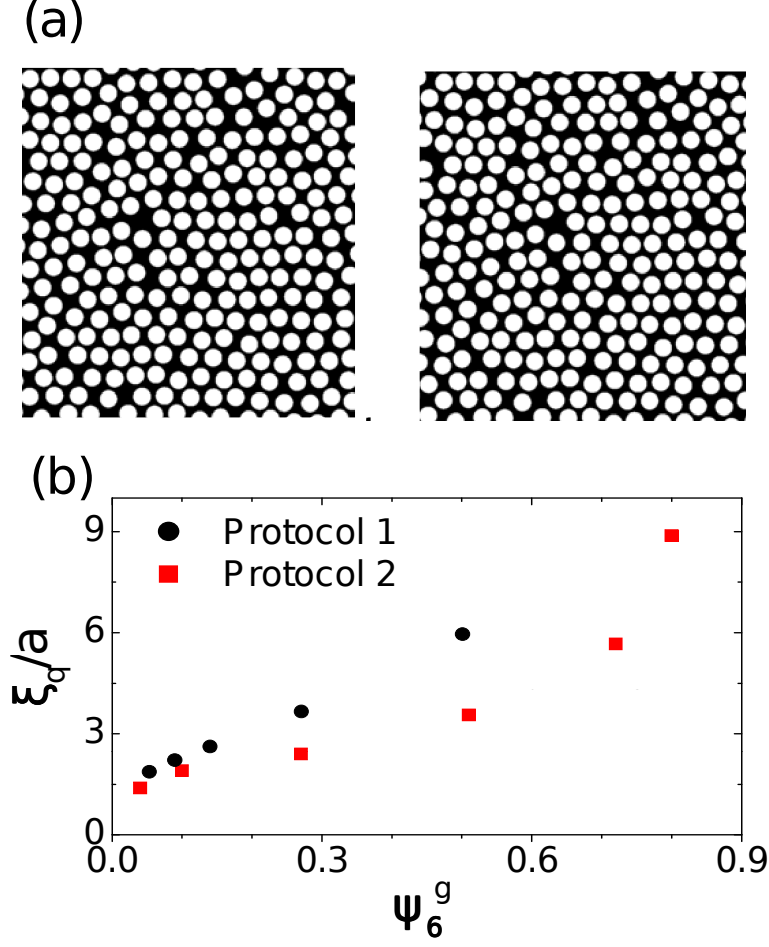


FIG. 4. (a) Equilibrated liquid configurations of cylinders generated with initial packing fractions $\phi_0 = 0.77$ (left) and 0.73 (right) and global bond-orientational order parameters $\psi_6^g = 0.80$ (left) and 0.27 (right). (b) Average domain size ξ_q versus ψ_6^g for configurations generated using protocols 1 and 2.

the structures generated by the first protocol with $p = 0.1, 0.2, 0.3, 0.4,$ and 0.5 , and a triangular lattice ($p = 0$) with identical density and diameter air cylinders. The refractive index of the dielectric host in which the air cylinders are embedded is also varied with $n = 3.4, 1.8,$ and 1.4 from left to right in Fig. 5. For $n = 3.4$ and $p = 0$, a complete depletion of the DOS from $a/\lambda = 0.235$ to 0.365 results from the full PBG between the first and second bands of the triangular lattice [Fig. 6(a)]. With the introduction of positional disorder, defect modes are created inside the gap, and the frequency region of depleted DOS becomes shallower and narrower. The higher frequency side of the gap (air band edge) is affected more than the lower frequency side (dielectric band edge). Because the air holes are

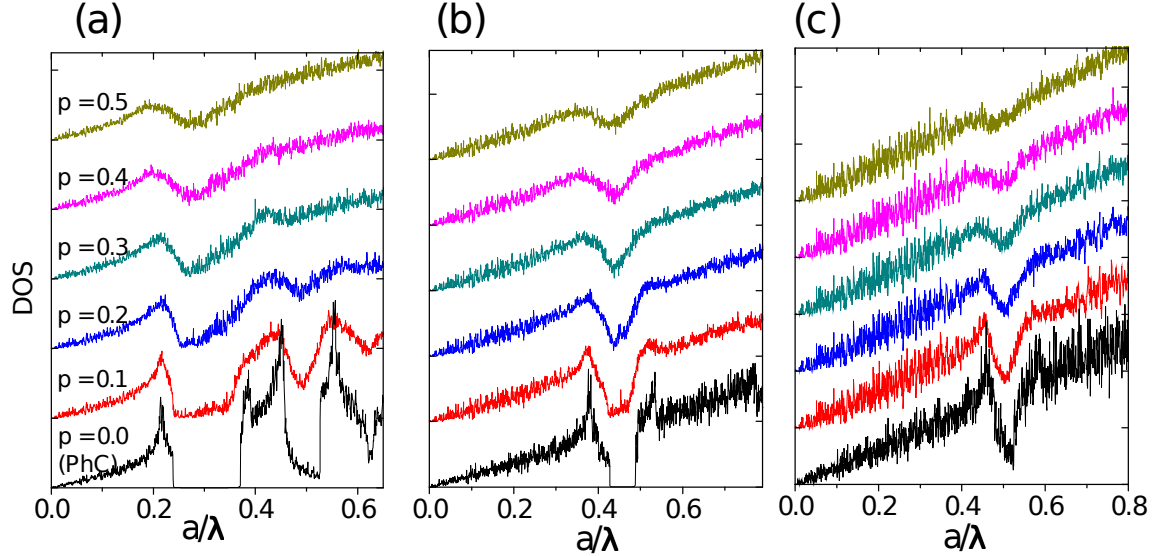


FIG. 5. Density of optical states (DOS) as a function of the normalized frequency $\omega_a/2\pi c = a/\lambda$ for the 2D structures generated by the first protocol with $p = 0.1, 0.2, 0.3, 0.4,$ and 0.5 , and a triangular lattice ($p = 0$ of identical density and diameter of air cylinders). The dielectric media, in which the air cylinders are embedded, have refractive indexes (a) 3.4, (b) 1.8, and (c) 1.4.

isolated and the dielectric host is connected, the dielectric bands below the gap are more robust to the disorder than the air bands above the gap. For $n = 1.8$, the PBG of the periodic structure becomes smaller, and thus the depleted region of the DOS is narrower. For the perfect crystal with $n = 1.4$, the first photonic band at the K point ($K1$) has the same energy as the second band at the M point ($M2$), thus the full PBG disappears. As a result, the DOS displays a dip, rather than a complete depletion. As shown in Fig. 5, the addition of positional disorder causes the dip in the DOS to become shallower and eventually disappear at large disorder.

To quantify the strength of the DOS depletion, we introduce the normalized depth S , which is defined as the ratio of the maximal depth of DOS reduction to the DOS of a random structure at the same frequency [Fig. 7(a)]. The density and diameter of air cylinders as well as the refractive index of the dielectric host in the random structure are identical to those of the structures under investigation. The DOS of the random structure increases almost linearly with frequency, similar to that of a homogeneous 2D dielectric medium. A linear fit of the DOS is shown as the red line in Fig. 7(a). We investigated the dependence of S on various order parameters, e.g. the local bond orientational order ψ_6^l . As shown in

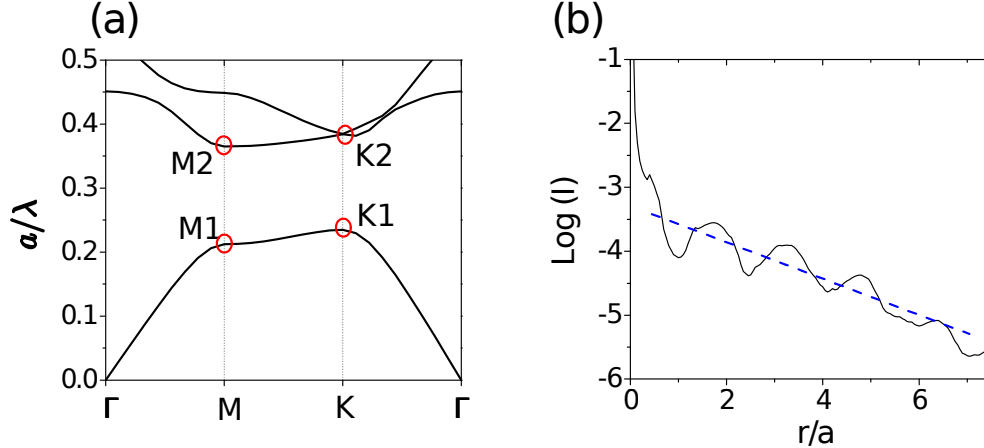


FIG. 6. (a) Photonic bands for a triangular array of air cylinders in a dielectric medium of refractive index $n = 3.4$. The cylinder radius $r = 0.37a$, where a is the lattice constant. (b) Logarithmic plot of the angle-averaged electric field intensity I versus the distance r from a dipole source oscillating at frequency $\omega_d = 0.51$ in the middle of a large triangular array. The dashed line is a fit to $\exp[-r/l_b]$, where l_b is the Bragg length.

Fig. 7(b), S increases gradually with ψ_6^l . However, the variation depends on the refractive index contrast n , and is therefore not universal.

To obtain universal behavior for a given degree of positional order, we must account for the effect of refractive index contrast on the DOS. The refractive index contrast determines the strength of the PBG, which is reflected in the attenuation length of Bragg diffraction, or the Bragg length l_b . Roughly speaking, the Bragg length gives an order of magnitude estimate for the minimal size of a periodic structure that is necessary to form a PBG via Bragg scattering. Since periodic structures are anisotropic, l_b varies with direction. However, since the DOS is a sum of optical modes in all directions, the relevant Bragg length is an average over all directions. To obtain the value of l_b in the numerical simulations, we place a continuous dipole source of frequency ω_d in the middle of a large triangular array of air cylinders. We then calculate the electric field intensity at a distance r from the source, and integrate it over the polar angle. The Bragg length l_b is extracted from the exponential decay of the angle-integrated field intensity I with r , as shown in Fig. 6 (b).

In Fig. 8(a), we plot the depth S versus the average size of the ordered domains normalized by the Bragg length, ξ_q/l_b . All data points for different refractive index contrasts fall on a single curve. When ξ_q/l_b is above a threshold value (~ 5), S is almost unity, which implies

that the depletion in the DOS is nearly complete as in a perfect crystal. When $\xi_q/l_b \lesssim 5$, S decreases rapidly. The drop can be fit by a straight line on a log-log plot, which reveals a power-law decay with an exponent ~ 0.52 . This result can be understood qualitatively as follows. If the domain size is larger than the Bragg length, Bragg scattering in a single domain is strong enough to form a PBG. The DOS in systems with large ξ_q/l_b is nearly equal to the DOS of a perfect crystal, and these structures can be regarded as photonic polycrystals. In addition, an average over many domains of different orientations makes the directional DOS isotropic. If the domain size is smaller than the Bragg length, individual domains are too small to form PBGs. In this case, the effect of Bragg scattering is reduced due to a limited number of periodic units, and the depletion of the DOS is weakened. This is the amorphous photonic regime, where short-ranged order leads to a partial depletion of the DOS. The well-defined threshold in ξ_q/l_b demonstrates a clear and sharp transition from polycrystalline to amorphous photonic structures.

In addition to the depth of the DOS reduction, we also studied the spectral width of the reduction region. The relative width w is defined as the ratio of the full width at half minimum (FWHM) of the dip in the DOS $\delta\omega$ to the frequency ω_0 at the center of the dip. Since the Bragg length varies within the spectral region of DOS reduction, we average its value over the frequency range from $\omega_0 - \delta\omega$ to $\omega_0 + \delta\omega$. The average domain size is normalized by the average Bragg length l_v . Figure 8 (b) shows a plot of w versus ξ_q/l_v for several values of n . Although the curves for different n do not coincide, their trends are similar. As ξ_q/l_v increases, w first drops and then rises (except for $n = 1.4$). The turning point is at $\xi_q/l_v \sim 1$. To understand this behavior, we first examine the DOS for periodic systems. At $n = 3.4$, the DOS is enhanced at the photonic band edges due to the slow group velocity [Fig. 5 (a)]. When positional disorder is introduced to the structure, the DOS peak at the air band edge is quickly lowered and the higher frequency part of the PBG is filled by defect modes. In contrast, the peak at the dielectric band edge decreases more slowly, because the dielectric bands are more robust against disorder as mentioned earlier. The gap width is reduced, until the DOS peak at the dielectric band edge diminishes at a certain degree of disorder. Then the DOS below the dielectric band edge starts decreasing with further increases in disorder. The DOS reduction region becomes wider. As n decreases, the strength of DOS reduction by PBGs is weakened, and $\delta\omega/\omega_0$ is lowered. At $n = 1.4$, w no longer rises beyond $\xi_q/l_v \sim 1$; instead it tends to a plateau.

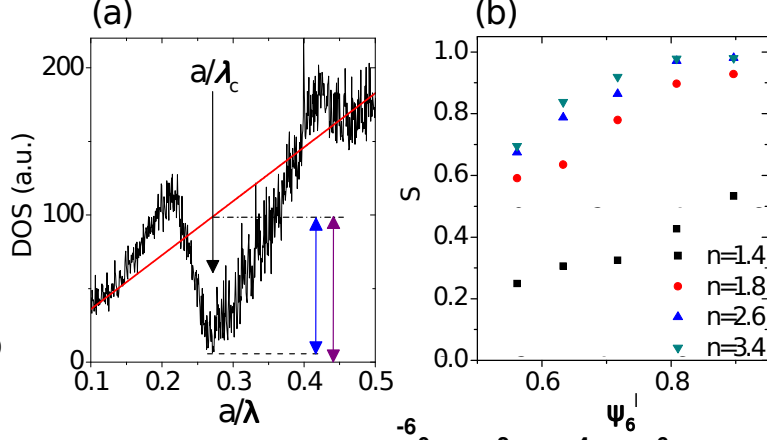


FIG. 7. (a) A schematic defining the normalized depth S , which is the ratio of the maximal reduction depth of the DOS (black curve) at frequency a/λ_c (blue segment with arrows) to the DOS of a random structure (fitted by the red solid line) at the same frequency (purple segment with arrows). (b) S versus the local bond-orientational order parameter ψ_6^l for arrays of air cylinders in a dielectric host of refractive index $n = 1.4, 1.8, 2.6,$ and 3.4 .

To check the robustness of our results on the method for generating configurations, we also calculated the DOS for structures produced by the second protocol. Figure 9 compares the normalized depth S and relative width w of the DOS reduction regions for the structures generated by the two protocols at $n = 3.4$. All data points for S versus ξ_q/l_b fall on the same curve in Fig. 9 (a). The data for w versus ξ_q/l_v for the two protocols display a similar trend as shown in Fig. 9 (b); however, the turning point is slightly shifted, and the values of w beyond the turning point are smaller for the structures produced by the second protocol. A more quantitative comparison will be carried out in the future.

IV. ENHANCED SCATTERING AND MODE CONFINEMENT BY SHORT-RANGE ORDER

In nature, the refractive index contrast is typically low, nevertheless photonic amorphous structures are used to manipulate light scattering and color generation. In this section, we investigate the effects of short-range order on light scattering and mode confinement in amorphous structures with low index contrast. We consider the structures generated by the first protocol with $p = 0.5$. When we set $n = 1.4$, the DOS possesses an extremely shallow

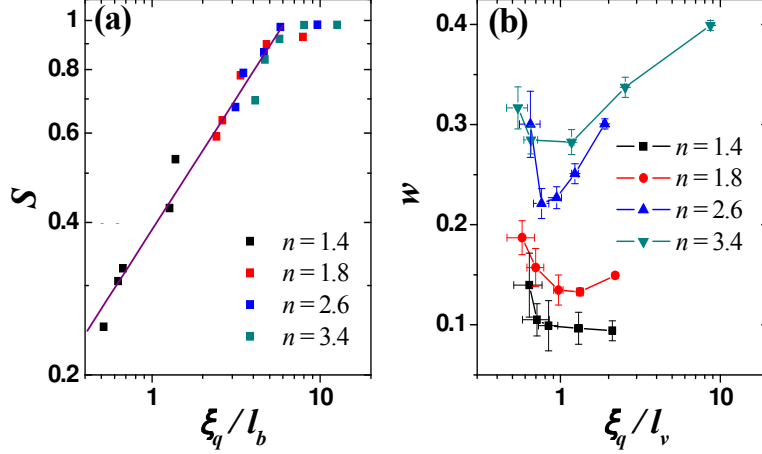


FIG. 8. (a) Normalized depletion depth of the DOS S for arrays of air cylinders in a dielectric host of refractive index n versus the ratio of the average domain size ξ_q to the angle-averaged Bragg length l_b . A linear fit (solid purple line) of the data on the log-log plot for $\xi_q/l_b \lesssim 5$ gives a power-law scaling exponent of 0.52. (b) Relative width w of the frequency region where there is a reduction in the DOS as a function of ξ_q/l_v , where l_v is the frequency- and angle-averaged Bragg length. The error bars are obtained from the standard deviation of ξ_q for different configurations and fitting errors in the FWHM of the DOS reduction zones.

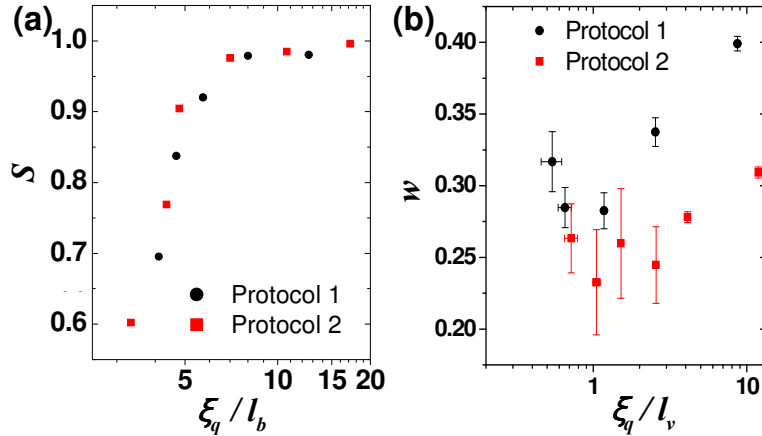


FIG. 9. Normalized depth S (a) and width w (b) of the DOS reduction region for the structures generated by protocols 1 (circles) and 2 (squares). The refractive index of the dielectric host, within which air cylinders, is $n = 3.4$. The horizontal axes are identical to those in Fig. 8 (a) and (b). The error bars in (b) are obtained using the same method in Fig. 8(b).

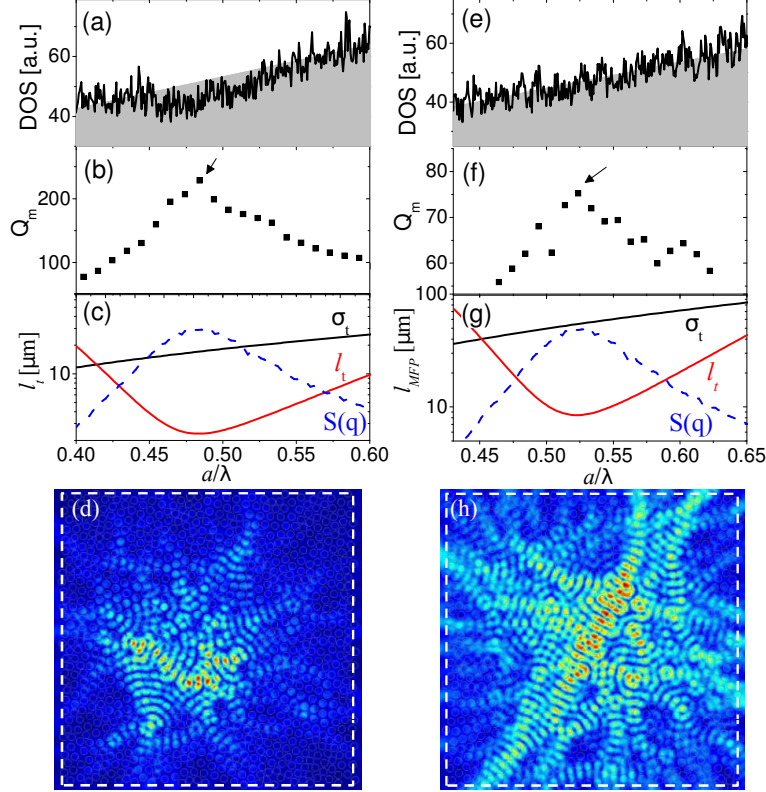


FIG. 10. The DOS (a,e) and maximal quality factors Q_m of resonant modes (b,f) for the amorphous photonic structures with low refractive index contrast $n = 1.4$ for (a-d) and 1.2 for (e-h). Grey backgrounds in (a,e) represent the DOS for 2D homogeneous media. (d,h): Spatial distribution of electric field intensities for the modes of maximal Q_m [marked by arrows in (b,f)]. (c,g): Transport mean free path l_t (red solid line), total scattering cross sections of a single scatterer σ_t (black dotted line), and the structure factor $S(q)$ at $q = 2k$ (blue dashed line), where k is the wavevector of light.

dip as shown in Fig. 10(a). For $n = 1.2$, the DOS in Fig. 10(e) is nearly featureless. We calculate the resonant modes in these structures using the finite element method. Instead of periodic boundary conditions, the structures have finite size and open boundaries. Each structure contains 1024 air cylinders in a dielectric medium. The open boundaries are terminated by perfectly matched layers that absorb all outgoing waves. Because of light leakage from the finite-sized structure, the resonant modes have finite lifetimes. We calculate the complex frequencies of all resonances $\omega_r + i\omega_i$. The amplitude of ω_i is inversely proportional to the lifetime. The quality factor is defined as $Q = \omega_r/2|\omega_i|$. We obtain the maximal quality factors Q_m of modes within small frequency intervals, and plot them in Fig. 10(b,f).

Although the dip in the DOS is barely visible at $n = 1.4$, Q_m is enhanced by a factor of three at a frequency near the center of the dip. Further, even though there is essentially no dip in the DOS for $n = 1.2$, Q_m displays a peak. Figure 10 (d,h) shows the spatial distributions of electric field intensities $|E(x, y)|^2$ for the modes with maximal Q_m (marked by the arrows in Fig. 10(b,f)). It is evident that the mode of maximal Q_m at $n = 1.4$ is localized within the structure. For $n = 1.2$ the mode is more delocalized, but the field intensity near the boundary (marked by white dashed line) is still weaker than that in the interior. To determine the degree of localization, we calculate the inverse participation ratio for these two modes,

$$s \equiv \frac{1}{L^2} \frac{(\int |E(x, y)|^2 dx dy)^2}{\int |E(x, y)|^4 dx dy}, \quad (6)$$

where a mode uniformly distributed over the sample gives $s = 1$. We find that the mode in Fig. 10(d) has $s = 0.18$ and is thus highly localized, while the one in Fig. 10(f) has $s = 0.44$ and is only partially localized.

To illustrate the physical mechanism that leads to mode confinement, we calculate the transport mean free path

$$\frac{1}{l_t} = \frac{\pi}{k^6} \int_0^{2k} \rho F(q) S(q) q^3 dq, \quad (7)$$

where k is the wavevector of light, ρ is the number density of air cylinders, $S(q)$ is the structure factor, $F(q)$ is the form factor, and q is the spatial frequency. $F(q)$ is given by the differential scattering cross section of a single air cylinder in the dielectric medium. The structure factor is given by

$$S(\mathbf{q}) \equiv \frac{1}{N} \sum_{i,j=1}^N e^{i\mathbf{q}\cdot(\mathbf{r}_i - \mathbf{r}_j)}, \quad (8)$$

where \mathbf{r}_i denotes the center position of the i th cylinder. Since the structures are isotropic, $S(\mathbf{q})$ is invariant with the direction of \mathbf{q} and is only a function of the magnitude q . In Fig. 10(c,g), we show that l_t displays a significant drop at a frequency that coincides with the peak in Q_m . This indicates that the enhancement of scattering strength improves mode confinement. In Fig. 10(c,g) we also plot the total scattering cross section σ_t of a single air cylinder, which increases monotonically with frequency and does not exhibit any resonant behavior within the frequency range studied. This behavior suggests that the dip in l_t is not caused by Mie resonance of individual scatterers. Instead, we contend that the short-range order enhances Bragg backscattering at certain wavelengths and shortens l_t . To prove this, we also plot $S(q)$ for the backscattering $q = 2k$ in Fig. 10 (c) and (g). $S(q)$ is peaked at

the dip of l_t , which confirms that collective backscattering from local domains of ordered cylinders causes a dramatic decrease in l_t . Therefore, the spatial confinement of resonant modes is enhanced by short-range order through constructive interference of scattered light that occurs at specific frequencies.

V. CONCLUSION

We generated polycrystalline and amorphous photonic structures using two protocols: one that produced jammed packings of cylinders and another that sampled equilibrated liquid states of cylinders. The degree of positional order was fully characterized by spatial correlation functions, Fourier power spectra, radial distribution functions, and bond-orientational order parameters. We were able to gradually decrease the average domain size and trace the transition from polycrystalline to amorphous media. The properties of the DOS were calculated for air cylinders embedded in a dielectric host with a refractive index contrast that varied from $n = 1.4$ to 3.4 . For $\xi_q/l_b \gtrsim 5$, where ξ_q is the average domain size and l_b is the angle-integrated Bragg length, the maximal depth of the DOS depletion is nearly unchanged from that for the crystalline structure. This is the polycrystalline regime, where individual domains are large enough to form PBGs. When $\xi_q/l_b \lesssim 5$, Bragg scattering from single domains is too weak to form PBGs, and the gap in the DOS diminishes. The spectral region of the DOS reduction first narrows with increasing disorder, then widens when the average domain size becomes less than the angle- and frequency-averaged Bragg length. These results can be explained by the increase of the DOS inside the gap due to defect modes and the decrease of the DOS outside the gap once the band edge modes with slow group velocities are destroyed by disorder. The behavior of the DOS is similar for structures generated by two qualitatively different protocols.

We also investigated the enhancement of light scattering and mode confinement in photonic amorphous structures with low-refractive index contrast. Even though the PBG effect is barely visible in the DOS, the transport mean free path displays a dramatic reduction and the quality factors of resonances reach a maximum. The short-range structural order enhances collective scattering of light and improves mode confinement. Therefore, in addition to the form factor or Mie resonances of individual scatterers, tailoring the structure factor is an efficient way of manipulating light scattering and confinement in photonic materials.

The authors thank Profs. Eric R. Dufresne and Richard O. Prum for stimulating discussions. This work is funded by NSF Grant Nos. DMR-0808937 (HC) and DMS-0835742 (CO, CS), and a seed grant from the Yale MRSEC (DMR-0520495). J.-K. Yang acknowledges the support of the National Research Foundation of Korea Grant funded by the Korean Government [NRF-2009-352-C00039]. This work also benefited from the facilities and staff of the Yale University Faculty of Arts and Sciences High Performance Computing Center and NSF grant No. CNS-0821132 that partially funded acquisition of the computational facilities.

-
- ¹ J.D. Joannopoulos, S. Johnson, J. Winn, and R. Meade, *Photonic Crystals: Molding the Flow of Light* (Princeton University Press, Princeton, 2008).
 - ² C.M. Soukoulis (ed.), *Photonic Crystals and Light Localization in the 21st Century* (Kluwer Academic, Norwell, 2001).
 - ³ S. Noda and T. Baba (eds.), *Roadmap on Photonic Crystals* (Kluwer Academic, Dordrecht, 2003).
 - ⁴ E. Yablonovitch, *Phys. Rev. Lett.* **58**, 2059 (1987).
 - ⁵ S. John, *Phys. Rev. Lett.* **58**, 2486 (1987).
 - ⁶ C. Jin, X. Meng, B. Cheng, Z. Li, and D. Zhang, *Phys. Rev. B* **63**, 195107 (2001).
 - ⁷ J. Ballato, J. Dimasio, A. James, and E. Gulliver, *Appl. Phys. Lett.* **75**, 1497 (1999).
 - ⁸ C. Rockstuhl, U. Peschel, and F. Lederer, *Opt. Lett.* **31**, 1741 (2006).
 - ⁹ Y. Wang and S. Jian, *Phys. Lett. A* **352**, 550 (2006).
 - ¹⁰ C. Rockstuhl, U. Peschel, and F. Lederer, *Phys. Rev. B* **79**, 132202 (2009).
 - ¹¹ P. D. García, R. Sapienza, Á. Blanco, and C. López, *Adv. Mater.* **19**, 2597 (2007).
 - ¹² K. Edagawa, S. Kanoko, and M. Notomi, *Phys. Rev. Lett.* **100**, 013901 (2008).
 - ¹³ M. Florescu, S. Torquato, and P. Steinhardt, *Proc. Nat. Aca. Sci. Am.* **106**, 20658 (2009).
 - ¹⁴ M. Rechtsman, A. Szameit, F. Dreisow, M. Heinrich, R. Keil, S. Nolte, and M. Segev, unpublished.
 - ¹⁵ P. Vukusic and J. Y. Sambles, *Nature* **424**, 852 (2003).
 - ¹⁶ S. Kinoshita and S. Yoshioka, *Chem. Phys. Chem.* **6**, 1442 (2005).
 - ¹⁷ R. O. Prum, in *Bird coloration*, Eds: G. E. Hill and K. J. McGraw (Harvard University Press,

- Cambridge, MA, 2006), Vol. 1, pp. 295353.
- ¹⁸ K. Kertész, Z. Bálint, Z. Vértesy, G. I. Márk, V. Lousse, J. P. Vigneron, M. Rassart, L. P. Biró, *Phys. Rev. E* **74**, 021922 (2006).
- ¹⁹ E. R. Dufresne, H. Noh, V. Saranathan, S. G. J. Mochrie, H. Cao, and R. O. Prum, *Soft Matter* **5**, 1792 (2009).
- ²⁰ H. Noh, S. F. Liew, V. Saranathan, S. G. J. Mochrie, R. O. Prum, E. R. Dufresne, and H. Cao, *Adv. Mater.* **22**, 2871 (2010).
- ²¹ L. F. Rojas-Ochoa, J. M. Mendez-Alcaraz, J. J. Sáenz, P. Schurtenberger, and F. Scheffold, *Phys. Rev. Lett.* **93**, 073903 (2004).
- ²² A. Derode, V. Mamou, and A. Tourin, *Phys. Rev. E* **74**, 036606 (2006).
- ²³ M. Reufer, L. F. Rojas-Ochoa, S. Eiden, J. J. Sáenz, and F. Scheffold, *Appl. Phys. Lett.* **91**, 171904 (2007).
- ²⁴ Y. Takeoka, M. Honda, T. Seki, M. Ishii, and H. Nakamura, *Appl. Mater. Inter.* **5**, 982 (2009).
- ²⁵ G.-J. Gao, J. Blawdziewicz, and C. S. O'Hern, *Phys. Rev. E* **74** (2006) 061304.
- ²⁶ P. J. Steinhardt, D. R. Nelson, and M. Ronchetti, *Phys. Rev. B* **28** 784 (1983).
- ²⁷ C. T. Chan, Q. L. Yu, and K. M. Ho, *Phys. Rev. B* **51**, 16635 (1995).
- ²⁸ E. Lidorikis, M. M. Sigalas, E. N. Economou, and C. M. Soukoulis, *Phys. Rev. B* **61**, 13458 (2000).
- ²⁹ J. Q. Broughton, G. H. Gilmer, and J. D. Weeks, *Phys. Rev. B* **25**, 4651 (1982).